Guidelines for QSM phantom production and evaluation of candidate phantom materials

Padriac Hooper[1,2], Jin Jin[1,2,3], Kieran O'Brien[1,2,3], Monique Tourell[1,2], Simon Daniel Robinson[2,4,5], and Markus Barth[1,2,6]

[1] ARC Training Centre for Innovation in Biomedical Imaging Technology, Brisbane, Australia,
[2] Centre for Advanced Imaging, The University of Queensland, Brisbane, Australia,
[3] Siemens Healthcare Pty Ltd, Brisbane, Australia,
[4] High Field MR Center, Department of Biomedical Imaging and Image-Guided Therapy, Medical University of Vienna, Austria,
[5] Christian Doppler Laboratory for MR Imaging Biomarkers, Department for Biomedical Imaging and Image-Guided Therapy, Medical University of Vienna, Austria,
[6] School of Information Technology and Electrical Engineering, The University of Queensland, Brisbane, Australia

Corresponding author: Markus Barth; m.barth@uq.edu.au.

Word count: 4,984 words

Submitted to Magnetic Resonance in Medicine.

Abstract

Purpose Quantitative susceptibility mapping (QSM) is an MR technique that depicts and precisely quantifies spatial biodistributions from MR phase images. Recently, QSM has gained much uptake as method for mapping iron and identifying calcium. However, QSM as a quantitative method needs an objective reference to assess its accuracy. Here we present guidelines for reproducible workflows for QSM phantom design and production to help standardization efforts and provide characterizations and recommendations for iron- and calcium-based materials given the repeatability and reproducibility.

Methods 5 concentrations of 4 materials (USPIO, ferritin, calcium chloride, calcium carbonate) were imaged with a multi-echo gradient-echo acquisition at 3 and 7 Tesla. Magnetic susceptibility and R2* relaxivity as well as intra-session, inter-session repeatability, inter-scanner reproducibility and molar susceptibility by QSM were quantified.

Results The QSM measurements of USPIO had a moderate to good inter-session repeatability. The molar susceptibility was approximately 2.45 times larger at 3 T compared to 7 T. The QSM measurements of ferritin had excellent inter-session repeatability. The molar susceptibility was approximately 4 % larger at 3 T compared to 7 T. The QSM measurements of calcium chloride had excellent inter-session repeatability and excellent inter-scanner reproducibility. The QSM measurements of calcium carbonate had a good to excellent inter-session repeatability and an excellent inter-scanner reproducibility.

Conclusion This work reveals ferritin and calcium chloride to be the most repeatable and reproducible iron-and calcium-based materials for QSM, respectively. A detailed methodology for phantom production, concentration ranges, visual analysis and statistical analysis are provided.

1 Introduction

Quantitative Susceptibility Mapping (QSM) allows non-invasive measurement of magnetic susceptibility sources[1,2]. QSM provides a novel predictive biomarker for a range of neural disorders. By mapping iron within deep grey matter structures, QSM has proven to be useful in the diagnosis and management of neurodegenerative disease[3]. Since QSM can distinguish between calcifications and hemorrhages, it can be used in tumor classification and assess microbleeds in traumatic brain injury patients[4, 5]. However, QSM contains several image processing steps to process the tissue susceptibility information from the phase, of which the optimal processing is unknown. In QSM, field changes are first detected following a very specific acquisition protocol [6, 7]. The phase must be reconstructed from individual coils without fringe lines, then precisely unwrapped to reveal the true range of phase variation [8]. From the fieldmap, background fields arising from large susceptibility sources are then corrected. These sources manifest as slowly varying fields that extend throughout the brain and obscure small susceptibility sources. The background fields are estimated by making an assumption about the background and/or local fields, and usually require a region-of-interest (ROI) defined by a mask input[9]. Given an accurate local field estimate, the magnetic susceptibility of the sample can be determined by a convolution operation with a dipole kernel[10, 11]. This corresponds to multiplication in the frequency space, where the divisor is undefined for angles approximating 54.7°. Various approaches impose sparsity or smoothness constraints with L1-norm or L2-norm regularizations. Some authors propose using prior information from the magnitude image[12], of the inverse phase noise[13, 14], or a reference tissue[15]. Another research group proposed to solve the spatial frequencies associated with the well-posed first, yielding prior information to help solve the ill-posed problem[16]. Too much regularization can result in bias due to over-fitting of QSM values, but not enough regularization can result in streaking artefacts.
Thus given the uncertainties in QSM reconstruction, work has begun on reaching a consensus for neuroimaging applications[7, 17, 18]. Widespread uptake and standardization requires the development of a known truth to assess bias, linearity and precision of measurements with a high level of certainty[19, 20], which can be achieved by the use of test objects with known quantities or phantoms. Traditionally, phantoms require tissue-mimicking materials capture relaxation times, dielectric values, and to provide stability over long periods[21]. However, for QSM phantoms, additional requirements include both paramagnetic and diamagnetic phantom materials to cover the ranges of magnetic susceptibility found in vivo. Of interest to QSM applications are the deep grey matter structures, iron-laden lesions and calcified lesions[2]. Therefore, QSM phantoms should aspire to mimic these structures within a single test object.

The first objective was to provide a detailed methodology for QSM phantom design and production. This involved providing a reproducible workflow for machining the phantom within a workshop and providing guidelines for septic production within a laboratory environment. The second objective was to examine the suitability of calcium-based and iron-based materials, characterise their magnetic susceptibility at field strengths of 3 Tesla and 7 Tesla, and investigate their repeatability and reproducibilty.

2 Methods

2.1 Phantom design and production

The design factors for producing the QSM phantom consisted of the following: (i) fitting within tight head coil setups, (ii) B_0/B_1 inhomogeneities at the phantom periphery, (iii) air bubble trapping, and (iv) long-term stability. To ensure fitting with the tight setup of the 7 Tesla Nova Medical head coil, the phantom was measured prior to construction and fitted (see Figure 1). To reduce B_0 and B_1 artefacts, vials were positioned at least 10 mm away from the phantom periphery. To trap air bubbles from the surrounding liquid, a small hole was drilled into the top supporting plate, creating a bubble trapping zone (see Figure 1).

Long-term stability was ensured by using agarose agarose gel for particle stability[22]. Milli-Q water was used since it did not contain metal ions or microbes that might contaminate the agarose or PVP-40 gel. The tight-fitting non-magnetic closure and NMR tube cap prevented microbes from entering the phantom and samples, respectively. Particle agglomerates were controlled by slow gel cooling and visual inspection.

Choosing materials of biologically relevant materials and susceptibilities was an unknown prior to this study. Therefore, the phantom was divided into four quadrants to determine the most suitable of two iron- and two calcium-based materials. 5 measurand levels were required to determine the slope between material concentration and QSM in accordance with recommendations from the Quantitative Imaging Bioalliance[19].

Iron-based phantoms were made by mixing hot agarose gel (A4018, Merck & Co.) solutions with Ultra-small SuperParamagnetic Iron Oxide (USPIO) nanoparticles or ferritin. USPIO (Molday Ion CL30Q02-2, BioPAL) concentrations were 0.224 to 0.672 micromoles of iron per millilitre (μM). Ferritin (F4503, Merck & Co.) concentrations were 3.76 to 10.21 μM. The concentrations were spaced equidistantly. USPIO nanoparticles were chosen due to their widespread use as novel MR contrast agents in neuroimaging, and their prior use with both QSM[23, 24]. Ferritin was chosen due to its biological relevance as a dominant form of susceptibility confirmed by biochemical analysis on iron-laden tissue[25].

Calcium-based phantoms were made by mixing hot agarose gel solutions with calcium carbonate ($CaCO_3$) or calcium chloride ($CaCl_2$). The powders of $CaCl_2$ (746495, Merck & Co.) and $CaCO_3$ (C4830, Merck & Co.) were each mixed with hot gel to make 0.9 to 4.5 and 1.0 to 5.0 millimoles per milliliter (mM), respectively. The concentrations were spaced equidistantly. $CaCO_3$ was chosen due to its presence in biochemical analyses within mineralizations and calcifications[26–28]. $CaCl_2$ was chosen due to its homogeneity in QSM maps at 3T[29].

The phantom was constructed from 20 nuclear magnetic resonance (NMR) vials (10 mm outer diameter, N-51A, Kimble Glass). To reduce standing waves and chemical shift artefacts at 7T, the phantom was filled with a solution of Milli-Q water, containing 44.3 weight percentage (wt.%) polyvinylpyrrolidone-40 (PVP-40, Merck & Co.) and 1.7 wt.% sodium chloride (NaCl, Merck & Co.) to mimic the electric permittivity and conductivity of white matter at approximately 7T. The phantom was given at least 48 hours for the PVP-NaCl mixture to settle before scanning[30].

Table 1: Acquisition, online reconstruction parameters and head coil used on the MR scanners.

	3 T Siemens	**7 T Siemens**
Model	Magnetom Prisma	Magnetom 7 T Plus
Gradient readout	Bipolar	Bipolar
TE_1:Δ TE:TE_{last}; TR (ms)	1.87:1.87:22.44; 26	3.15:3.15:28.35; 32
Coil	20-ch Rx head coil	32-ch Rx head coil
Voxel size	1.0 mm^3 isotropic	0.7 mm^3 isotropic
Acquisition matrix	$192 \times 192 \times 104$	$272 \times 272 \times 160$
Flip angle; Bandwidth; Averages	15°;1000 Hz/pix; 1	15°;340 Hz/pix; 1
Acceleration type and factor	not used	GRAPPA 2
Distortion correction	not used	2D distortion correction
Partial Fourier factor; Elliptical scanning	not used;not used	6/8 PFA; used
Prescan normalize correction	used	not used

2.2 MR data acquisition

The phantom was scanned at 3T and 7T within a 20-channel and 32-channel head coil respectively. Phase and magnitude images were acquired with a multi-echo 3D gradient-echo sequence using the parameters shown in Table 1. B_0 shimming was performed using the vendor's sequence: *GRE brain*. For estimation of signal-to-noise (SNR), another acquisition was conducted with all imaging filters and acceleration off. Two scans (test-retest) were acquired at the baseline time-point for intra-session repeatability. The 5 $CaCO_3$ vials were included in the phantom 9 months after baseline. The phantom was scanned again at the 9 months time-point, then again twice (test-retest) after 24 months.

2.3 SNR estimation

Signal-to-noise-ratio (SNR) was estimated by a two-region approach using a magnitude image acquired without parallel imaging or filters (distortion correction, partial Fourier, elliptical scanning, prescan normalize). Noise was estimated as the mean of the 4 magnitude image corners divided by a correction factor for Rayleigh distribution within multi-channel images[31]. SNR was used to threshold regions of low SNR as defined below in the analysis.

2.4 QSM reconstruction

Phase images were reconstructed on the scanners' image reconstruction computers using ASPIRE phase offset correction[32]. Thereafter, the full QSM reconstruction was performed in MATLAB R2021a (v9.10.0) using the SEPIA toolbox (v1.0.0) [33]. ROMEO total field calculation[34] (MriResearchTools v2.1.0) was used for masking, phase unwrapping, bipolar readout phase correction and echo combination[34]. Background fields were corrected with V-SHARP[35, 36] using a maximum spherical mean value (SMV) of 12 mm. A relative residual map was derived from the mono-exponential decay model, thresholding at 0.5[33]. This information was multiplied by the signal mask (removing the affected voxels) for the dipole inversion step. The dipole inversion problem was solved using rapid-two-step dipole inversion[16]. For calcium carbonate, later echo times were removed to ensure voxels with low SNR (SNR < 10) were not included in the analysis (section 3.3.3),

so the first 7 echoes at 3T and the first 3 echoes at 7T were included.

2.5 $R2^*$ mapping and region-of-interest (ROI) selection

$R2^*$ maps were generated by voxel-wise fitting using the auto-regression on linear operations (ARLO) algorithm[37]. The echo times selected in $R2^*$ mapping were the same echo times selected as those in QSM reconstruction for each material.
The co-registration and segmentation steps were performed within ITK-SNAP[38] version 4.0 (`http://www.itksnap.org`). The R2* maps at later time-points (9 and 24 months) were co-registered to the baseline R2* map, using mutual information as a similarity metric and linear interpolation to re-slice the images. The same rigid transformation parameters were applied to QSM maps. For each of the 20 vials, a segmentation was created by thresholding the $R2^*$ maps over 40 to 60 central slices. These segmentations were then multiplied by the mask to ensure affected voxels were removed.

2.6 Data analysis

The concentration (x-axis) and their uncertainties (error bar in x) was plotted against the average ROI mean across time-points (y-axis), and their standard deviations (error bar in y). Least-squares linear regression was used to fit concentration against the average ROI mean, and the coefficients were expressed in terms of point estimate (95 % confidence intervals).
Repeatability were assessed using the ROI mean from pairs of measurements on the same scanner. Intra-session repeatability was calculated from test-retest measurements. Inter-session repeatability was calculated from the baseline measurement and time-point measurements. The test-retest measurements were averaged for calculation of inter-session repeatability[39]. Intra- and inter-session repeatability was evaluated with interclass correlation coefficient (ICC). The ICC values were calculated using a two-way mixed-effect model, absolute agreement, multiple measurements (A-k)[40]. ICC values were expressed as 95% confidence intervals. The repeatability was classified as poor, moderate, good and excellent repeatability given ICC values less than 0.5, between 0.5 and 0.75, between 0.75 and 0.9, and greater than 0.90, respectively. ICC values needed to have small confidence intervals (CIs) to be considered as good or excellent[41]. The ICC values of inter-scanner measurements were reported only if there was not a statistically significant difference between inter-scanner measurements. A student's t-test was used to make this assessment. Statistical testing was conducted with a 5 % significance level using Microsoft Excel Version 2311 (Microsoft, Redmond, WA).

3 Results

3.1 Quantitative maps, susceptibility and relaxivity

The phantom went through multiple iterations prior to reaching the final version and these were conveyed in Figure 2. Various vial wall thicknesses (0.3 mm, 2 mm) were assessed. Figure 2 showed that for the high wall thickness, high R2* values and erroneous QSM values were observed. For the low wall thickness, the vial wall effects were not observed.
At 7 T, artefacts associated with the shorter RF wavelengths at 7 T were observed due to the unsuitable electric permittivity of the phantom. We attempted to correct for these artefacts by introducing

Table 2: Intra-session and inter-session repeatability measurements. Interclass coefficient (ICC) was expressed as a 95 % confidence interval.

	3 T	**7 T**	**3 T**	**7 T**
Iron-based materials	**USPIO**		**Ferritin**	
QSM-Intra-sess-ICC	1.000-1.000	0.999-1.000	1.000-1.000	1.000-1.000
QSM-Inter-sess-ICC	0.590-1.000	0.898-0.998	0.996-1.000	0.954-1.000
$R2^*$-Intra-sess-ICC	0.992-1.000	1.000-1.000	0.991-1.000	0.999-1.000
$R2^*$-Inter-sess-ICC	0.965-1.000	0.895-0.998	0.855-0.996	0.853-0.999
Calcium-based materials	**$CaCl_2$**		**$CaCO_3$**	
QSM-Intra-sess-ICC	1.000-1.000	1.000-1.000	0.983-1.000	0.992-1.000
QSM-Inter-sess-ICC	0.992-1.000	0.997-1.000	0.784-1.000	0.959-1.000
$R2^*$-Intra-sess-ICC	0.835-0.998	0.934-1.000	0.995-1.000	0.979-1.000
$R2^*$-Inter-sess-ICC	-0.198-0.764	-0.440-0.957	0.962-1.000	0.931-1.000

a PVP-40/NaCl mixture. However, some residual detergent caused chemical shift artefacts that caused destructive interference at 7 T. This was then corrected by replacing the mixture with a fresh PVP-40/NaCl batch.

Maps and plots of magnetic susceptibility and R2* relaxivity for the 4 used materials and 5 concentrations are shown in Figures 3,4,5,6. The fit results are listed in Table 3.

3.2 Iron-based materials

Agglomerates were observed in USPIO 0.448 μM vial, manifesting as bright on both the QSM and $R2^*$ maps on Figure 3. The QSM intercept was significantly different from zero at both field strengths (3 T: p = 0.035; 7 T: p = 0.009, 95 % significance level).
Ferritin concentrations 6.98, 8.60, 10.21 μM each exhibited agglomerates. These manifested as dark on the QSM map and bright on the $R2^*$ maps on Figure 4). The goodness-of-fit of iron concentration and QSM or $R2^*$ was excellent (adj-$R^2 > 0.9$) in all cases.

3.2.1 Intra- and inter-session repeatability

The intra-session repeatability of QSM measurements of iron-based materials was excellent in all cases (see Table 2). For USPIO, the inter-session repeatability of QSM measurements was moderate at 3 T (ICC = 0.590-1.000) and good at 7 T (ICC = 0.898-0.999). For ferritin, the repeatability of QSM measurements was excellent at both field strengths (3 T: ICC = 0.996-1.000; 7 T: ICC = 0.954-1.000).

3.2.2 Inter-scanner reproducibility

For the 5 USPIO concentrations, the inter-scanner QSM measurements were significantly different (p = 0.004). The molar susceptibility at 3 T (1.595 ppm.μM^{-1}) was 2.45 times larger than at 7 T (0.650 ppm.μM^{-1}). The inter-scanner reproducibility of $R2^*$ measurements was moderate (ICC

= 0.560-1.000). The $R2^*$ relaxivity at 3 T (67.0 $s^1.\mu M^{-1}$) was in close agreement to 7 T (66.6 $s^1.\mu M^{-1}$).

For the 5 ferritin concentrations, the inter-scanner QSM measurements were significantly different (p = 0.003). The inter-scanner $R2^*$ measurements were significantly different (p = 0.015). The molar susceptibility at 3 T (0.0915 ppm.μM^{-1}) was 3.7% larger than at 7 T (0.0902 ppm.μM^{-1}). The $R2^*$ relaxivity at 3 T (0.954 $s^{-1}.\mu M^{-1}$) was 2.98 times smaller than at 7 T (2.839 $s^{-1}.\mu M^{-1}$).

3.3 Calcium-based materials

At 7 T, shading at phantom periphery occurred due to the interaction between $CaCl_2$ conductivity and the B_1 field resulting in variations in $R2^*$ surrounding the $CaCl_2$ vials (see Figure 5). In the 7 T $R2^*$ and QSM maps on Figure 5, heterogeneity at $CaCl_2$ 4.5 mM was observed due to the solubility limit of $CaCl_2$ in aqueous solutions. Therefore, $CaCl_2$ 4.5 mM was removed from analysis. The goodness-of-fit of $CaCl_2$ concentration versus QSM was excellent (adj-$R^2 > 0.9$). The goodness-of-fit of $CaCl_2$ concentration versus $R2^*$ was poor at 3 T (adj-$R^2 < 0.5$) and moderate at 7 T (adj-$R^2 > 0.75$).

At both 3 T and 7 T, $CaCO_3$ 0.9 mM contained diamagnetic clumps (dark on QSM map, bright on R2* map) surrounded by a paramagnetic mixture (bright on QSM map, dark on R2* map) (see Figure 6). Accordingly, the QSM intercept was significantly different from zero at both field strengths (3 T: p = 0.016; 7 T: p = 0.018, 95 % significance level). The goodness-of-fit of $CaCO_3$ concentration versus QSM were excellent (adj-$R^2 > 0.9$). The goodness-of-fit of $CaCO_3$ concentration versus $R2^*$ were excellent (adj-$R^2 > 0.9$) and moderate (adj-$R^2 > 0.75$) at 3 T and 7 T, respectively.

3.3.1 Intra- and inter-session repeatability

For $CaCl_2$, the intra-session repeatability of QSM measurements was excellent at both field strengths (see Table 2). The inter-session repeatability of QSM measurements was excellent at both 3 T (ICC = 0.992-1.000) and 7 T (ICC = 0.997-1.000). The intra-session repeatability of $R2^*$ measurements was good at 3 T (ICC = 0.835-0.999) and excellent at 7 T (ICC = 0.934-1.000). The inter-session repeatability of $R2^*$ measurements was poor at both 3 T (ICC = -0.198-0.764) and 7 T (ICC = -0.440-0.957).

For $CaCO_3$, the intra-session repeatability of QSM measurements was excellent at both field strengths. The inter-session repeatability of QSM measurements was good at 3 T (ICC = 0.784-1.000) and excellent at 7 T (ICC = 0.959-1.000). The intra-session repeatability of $R2^*$ measurements was excellent at both 3 T (ICC = 0.995-1.000) and 7 T (ICC = 0.979-1.000). The inter-session repeatability of $R2^*$ measurements was excellent at both 3 T (ICC = 0.962-1.000) and 7 T (ICC = 0.931-1.000).

3.3.2 Inter-scanner reproducibility

For the 4 $CaCl_2$ concentrations, the inter-scanner reproducibility of QSM measurements was excellent (ICC = 0.999-1.000). The molar susceptibility at 3 T (-0.324 ppm.mM^{-1}) was in close agreement with 7 T (-0.328 ppm.mM^{-1}). The inter-scanner $R2^*$ measurements were significantly different

Table 3: Linear fitting coefficients for molar concentration versus QSM or $R2^*$. The slope (molar susceptibility or $R2^*$ Relaxivity) and intercept were given as point estimate (95% confidence interval).

	3 T	**7 T**	**3 T**	**7 T**
Iron-based	**USPIO**		**Ferritin**	
χ_M (ppm.μM^{-1})	1.595 (0.506)	0.650 (0.249)	0.0915 (0.0392)	.0902 (.0319)
Intercept (ppm)	0.28 (0.24)	0.23 (0.12)	0.10 (0.29)	0.06 (0.24)
Adjusted R-squared	0.961	0.936	0.931	0.952
Relaxivity (s^{-1}.μM^{-1})	67.0 (20.6)	66.6 (16.9)	0.954 (0.322)	2.839 (1.153)
Adjusted R-squared	0.968	0.979	0.953	0.942
Calcium-based	**$CaCl_2$**		**$CaCO_3$**	
χ_M (ppm.mM^{-1})	-0.324 (0.147)	-0.328 (0.127)	-0.1236 (0.0408)	-0.0945 (0.0333)
Intercept (ppm)	0.03 (0.36)	0.04 (0.31)	0.21 (0.13)	0.17 (0.12)
Adjusted R-squared	0.964	0.975	0.958	0.954
Relaxivity (s^{-1}.mM^{-1})	0.443 (1.403)	2.521 (1.332)	32.6 (9.3)	57.8 (4.58)
Adjusted R-squared	0.221	0.821	0.968	0.791

($p = 0.047$). On average, the $R2^*$ measurements at 3 T (12.8 ± 0.7 s^{-1}) were 1.4 s^{-1} lower than the $R2^*$ measurements at 7 T (14.2 ± 1.5 s^{-1}).
For the 5 $CaCO_3$ concentrations, the inter-scanner reproducibility of QSM measurements was good (ICC = 0.808-0.998). The molar susceptibility at 3 T (-0.1236 ppm.mM^{-1}) was 23 % higher than 7 T (-0.0945 ppm.mM^{-1}). The inter-scanner $R2^*$ measurements were significantly different ($p = 0.025$). The $R2^*$ relaxivity at 3 T (32.6 s^{-1}.mM^{-1}) was 1.77 times less than 7 T (57.8 s^{-1}.mM^{-1}.

3.3.3 SNR estimates

The SNR estimates at 3 T and 7 T are shown in Supporting Tables 1 and 2, respectively. For USPIO, ferritin and $CaCl_2$, the SNR was well above the low-SNR threshold (SNR < 10) for all echo times (TEs). However, for $CaCO_3$, rapid signal decay occurred due to low water proton density of the samples at all concentrations. At 3 T, for 3 mM and above, SNR was less than 10 at echo times TE_{8-12} (TE = 14.96 to 22.44 ms). Thus, echo times TE_{1-7} (TE = 1.87 to 13.09 ms) were chosen for inclusion of the $CaCO_3$ QSM and $R2^*$ reconstruction at 3 T. At 7 T, SNR was less than 10 for the 5 mM ROI at TE_2 (TE = 6.30 ms). In addition, SNR was less than 10 for the 4 and 5 mM concentrations at TE_3 (TE = 9.45 ms). With the caveat of low SNR at concentrations 4 and 5 mM, echo times TE_{1-3} (TE = 3.15 to 9.45 ms) were chosen for inclusion of the $CaCO_3$ QSM and $R2^*$ reconstruction at 7 T.

4 Discussion

The proposed phantom provides an exciting step towards building a ground-truth reference for QSM by characterising a range of relevant materials. The study evaluated the QSM relaxivity and repeatability of 4 materials using 5 measurand levels, following recommendations from the Quantitative Imaging Bioalliance (QIBA). The phantom had long-term stability over a period of 2 years. This was achieved by avoiding microbial growth, gel contraction and mitigating uncertainties from particle agglomerates. The next step would be to construct a more robust confidence interval by increasing

to at least 9 measurand levels for one calcium-based and one iron-based material, providing sufficient statistical power to assess bias and linearity. Such a phantom could be applied to assess the accuracy and precision of inter-scanner measurements, and for longitudinal studies to aid in clinical decision making.

Our study provides an important step for a stable QSM phantom using biologically relevant materials and susceptibilities. In terms of $R2^*$, QSM and field strength, the key findings are outlined as follows for each material:

1. **USPIO :** The QSM measurements had moderate to good inter-session repeatability. The molar susceptibility was approximately 2.45 times larger at 3T due to the magnetic saturation effect. The $R2^*$ measurements had good inter-session repeatability and moderate inter-scanner reproducibility.

2. **Ferritin :** The QSM measurements of ferritin had excellent inter-session repeatability. The molar susceptibility was approximately 3.7% larger at 3T.

3. **$CaCl_2$:** The QSM measurements had an excellent inter-session repeatability and an excellent inter-scanner reproducibility.

4. **$CaCO_3$:** The QSM measurements had a good to excellent inter-session repeatability. The molar susceptibility was approximately 31 % larger at 3T.

The molar susceptibility of fully loaded ferritin is approximately 0.0782 ppm.μM^{-1}[25]. Our molar susceptibility values were overestimated by 17% at 3T and by 15% at 7T. A phantom study by Olsson et al. investigated QSM reconstruction errors that occur within long cylinders oriented parallel to B_0[42]. In their work, they observed an overestimation relative to theoretical estimates of gadolinium of approximately 20 %, similar to the overestimation observed in our ferritin vials. This discrepancy can be due to the limitations of the infinite cylindrical model, with an analytical solution between the local field and the magnetic susceptibility as derived in [43] and shown in Supplementary Figure 1. For ferritin, the molar susceptibility by analytical estimate was 2% less at 3T and 3.2% less at 7T. Additional contribution factors to wrong estimations can be shading observed outside the vials in Figure 2 (K-L) were particularly prominent at large susceptibility values at 3 T, indicating unresolved external background fields influencing the QSM result.

Our findings indicated that QSM measurements from ferritin ROIs were more repeatable and reproducible than from USPIO ROIs. Similarly, they find that the QSM measurements from $CaCl_2$ ROIs were more repeatable and reproducible than from $CaCO_3$ ROIs. Future QSM phantoms should use agarose mixtures doped with ferritin and $CaCl_2$ to produce realistic paramagnetic and diamagnetic values respectively.
This study used QSM acquisition parameters that reflected those most commonly used for in vivo studies. The smaller voxel size at 7 T (0.7 mm^3) produced more precisely defined voxels than at

3 T (1.0 mm^3). Ferritin and $CaCO_3$ ROIs were heterogeneous due to agglomerates and sediments which may have contributed to the complexity of QSM reconstruction. Moreover, the voxel sensitivity function mixing effect at lower image resolutions reduces phase contrast, particularly at high susceptibilities[44]. At 3 T, it was difficult to observe the agglomerates and sediments, while at 7 T they were observed with clarity.

In-plane imaging artefacts were observed in the phantom. At 3 T, in-plane shading was observed in the annulus a few voxels surrounded the vials of high susceptibility on the QSM maps. AT 7 T, Gibbs ringing were observed a few voxels both within and outside the vials on the $R2^*$ maps. Gibbs ringing artefacts led to $R2^*$ mapping errors. These were minimized first by a relative residual mask of the $R2^*$ mono-exponential decay model, then by thresholding the $R2^*$ map during ROI selection.

A QSM phantom study involved a validation of mixed diamagnetic and paramagnetic susceptibility sources[45]. Their method required control of particle sizes to inter-disperse paramagnetic and diamagnetic particles. Another recent QSM phantom study involved a promising method to control the clustering of iron-based particles with hydrogels[46]. Our phantom used 20 vials with one material and concentration each within one phantom trying to optimize availabel space, compared to 9 vials in Cuna et al. and 10 vials in Emmerich et al. The design of our phantom could therefore be used for studies incorporating both para- and dia-magnetic materials at sample sizes 9-10 each. Moreover, each vial allows to include a large ROI with over 2000 voxels in the analysis, to help increase measurement precision. we also provide more detailed information about the phantom production production process on GitHub to encourage reproducible methods, provided there is access to a workshop and a laboratory.

Recommendations for developing a QSM phantom are provided below as follows: (i) Use PVP-40/NaCl mixtures to fill the phantom to minimize standing waves and avoid chemical shift artefacts at 7 T. (ii) When procuring samples, ensure there are no trace metals on the manufacturer's specifications. (iii) Use at least 9 samples each of ferritin and $CaCl_2$. Use ferritin concentrations between 0.9 to 2.7 μM to target the susceptibility of deep grey matter structures, then 3.6 μM and higher to target iron-laden lesions. Use $CaCl_2$ concentrations between 0.3 to 0.9 mM to target the susceptibility of calcifications and calcified lesions. Position vials of higher susceptibility towards the center of the phantom. (vi) Work together with a workshop to produce the phantom from our CAD designs and (vii) follow our guidelines for QSM phantom production within a septic lab environment.

5 Conclusions

This work presents a detailed account of the methodology for phantom production, measurement and analysis of a ground-truth reference for QSM and R2* and the associated challenges to obtain highly repoducible measurements. Our results for the tissue magnetic susceptibility and R2* relaxivity show the different field strength dependent behaviour of a range of materials relevant for the QSM and R2* relaxometry which will help in selecting the most suitable ones with regard to

mimicking tissue properties and phantom stability.

6 Data Availability Statement

We facilitate the reproducibility of this study and the phantom by providing instructions for phantom production, CAD files, imaging data and MATLAB scripts used for data analysis on the Github page (`https://github.com/paddyhooper93/QSM_Phantom`, commit hash 225327e).

Acknowledgments

We are grateful to Carl Dixon from the CAI workshop for engineering design input and for machining the phantom. We are appreciative of Kris Thurecht, Idriss Blakey and Craig Bell for their practical advice regarding agarose gel production. We thank Martijn Cloos for providing the CAD model of the 7 Tesla Nova Medical 32 RX-element coil. This work was published in preliminary form[47].

Conflict of interest

Kieran O'Brien and Jin Jin are employees of Siemens Healthineers in Australia. The remaining authors declare that the research was conducted in the absence of any commercial or financial relationship that could be construed as a conflict of interest.

Financial disclosure

This research was funded by the Australian Government through the Australian Research Council (project number IC170100035). The authors acknowledge the facilities and scientific and technical assistance of the NIF, a National Collaborative Re- search Infrastructure Strategy (NCRIS) capability, at the Univerity of Queensland. The financial support by the Austrian Federal Ministry for Digital and Economic Affairs, the National Foundation for Research, Technology and Development and the Christian Doppler Research Association is gratefully acknowledged.

CRediT author statement

Padriac Hooper: Conceptualization, Methodology (Phantom design and production, MR acquisition, uncertainty propagation analysis, QSM reconstruction, data analysis), Visualization, Writing - Original Draft, Figures 1-6, Review & Editing
Jin Jin: Methodology, MR acquisition, SNR estimation, Review & Editing
Kieran O'Brien: Conceptualization, Funding acquisition, Review & Editing
Monique Tourell: Methodology, MR acquisition, Review & Editing
Simon Robinson: Methodology, QSM reconstruction, Review & Editing
Markus Barth: Conceptualization, Methodology, Supervision, Review & Editing, Funding acquisition

7 References

[1] Eskreis-Winkler S, Zhang Y, Zhang J, et al. The clinical utility of QSM: disease diagnosis, medical management, and surgical planning *NMR in Biomedicine*. 2017;30:e3668.

[2] Wang Yi, Spincemaille Pascal, Liu Zhe, et al. Clinical quantitative susceptibility mapping (QSM): Biometal imaging and its emerging roles in patient care: Clinical QSM Biometals *Journal of Magnetic Resonance Imaging.* 2017;46:951–971.

[3] Ravanfar P, Loi SM, Syeda WT, et al. Systematic review: quantitative susceptibility mapping (QSM) of brain iron profile in neurodegenerative diseases *Frontiers in neuroscience.* 2021;15:41.

[4] Deistung A, Schweser F, Wiestler B, et al. Quantitative susceptibility mapping differentiates between blood depositions and calcifications in patients with glioblastoma *PloS one.* 2013;8:e57924.

[5] Bandt SK, Rochefort L, Chen W, et al. Clinical Integration of Quantitative Susceptibility Mapping Magnetic Resonance Imaging into Neurosurgical Practice *World Neurosurgery.* 2019;122:e10–e19.

[6] Haacke EM, Liu S, Buch S, Zng W, Wu D, Ye Y. Quantitative susceptibility mapping: current status and future directions *Magnetic resonance imaging.* 2015;33:1–25.

[7] Bilgic B, Costagli M, Chan K, et al. Recommended Implementation of Quantitative Susceptibility Mapping for Clinical Research in The Brain: A Consensus of the ISMRM Electro-Magnetic Tissue Properties Study Group *Magnetic resonance in medicine.* 2024.

[8] Robinson Simon Daniel, Bredies Kristian, Khabipova Diana, Dymerska Barbara, Marques José P., Schweser Ferdinand. An illustrated comparison of processing methods for MR phase imaging and QSM: combining array coil signals and phase unwrapping: Phase image combination and unwrapping *NMR in Biomedicine.* 2017;30:e3601.

[9] Schweser Ferdinand, Robinson Simon Daniel, De Rochefort Ludovic, Li Wei, Bredies Kristian. An illustrated comparison of processing methods for phase MRI and QSM: removal of background field contributions from sources outside the region of interest *NMR in Biomedicine.* 2017;30:e3604.

[10] Marques JP, Bowtell R. Application of a Fourier-based method for rapid calculation of field inhomogeneity due to spatial variation of magnetic susceptibility *Concepts in Magnetic Resonance Part B: Magnetic Resonance Engineering: An Educational Journal.* 2005;25:65–78.

[11] Salomir Rares, Senneville Baudouin Denis, Moonen Chrit TW. A fast calculation method for magnetic field inhomogeneity due to an arbitrary distribution of bulk susceptibility *Concepts in Magnetic Resonance.* 2003;19B:26–34.

[12] De Rochefort Ludovic, Brown Ryan, Prince Martin R, Wang YI. Quantitative MR susceptibility mapping using piece-wise constant regularized inversion of the magnetic field *Magnetic Resonance in Medicine: An Official Journal of the International Society for Magnetic Resonance in Medicine.* 2008;60:1003–1009.

[13] Liu Jing, Liu Tian, Rochefort Ludovic, et al. Morphology enabled dipole inversion for quantitative susceptibility mapping using structural consistency between the magnitude image and the susceptibility map *Neuroimage.* 2012;59:2560–2568.

[14] Milovic Carlos, Bilgic Berkin, Zhao Bo, Acosta-Cabronero Julio, Tejos Cristian. Fast nonlinear susceptibility inversion with variational regularization *Magnetic resonance in medicine.* 2018;80:814–821.

[15] Liu Zhe, Spincemaille Pascal, Yao Yihao, Zhang Yan, Wang Yi. MEDI+ 0: Morphology enabled dipole inversion with automatic uniform cerebrospinal fluid zero reference for quantitative susceptibility mapping *Magnetic resonance in medicine.* 2018;79:2795–2803.

[16] Kames Christian, Wiggermann Vanessa, Rauscher Alexander. Rapid two-step dipole inversion for susceptibility mapping with sparsity priors *Neuroimage.* 2018;167:276–283.

[17] Marques JP, Meineke Jakob, Milovic C, et al. QSM reconstruction challenge 2.0: A realistic in silico head phantom for MRI data simulation and evaluation of susceptibility mapping procedures *Magnetic Resonance in Medicine.* 2021;86:526–542.

[18] Langkammer C, Schweser F, Shmueli K, et al. Quantitative susceptibility mapping: Report from the 2016 reconstruction challenge *Magnetic resonance in medicine.* 2018;79:1661–1673.

[19] Raunig DL, McShane LM, Pennello G, et al. Quantitative imaging biomarkers: a review of statistical methods for technical performance assessment *Statistical methods in medical research.* 2015;24:27–67.

[20] Sullivan Daniel C., Obuchowski Nancy A., Kessler Larry G., et al. Metrology Standards for Quantitative Imaging Biomarkers *Radiology.* 2015;277:813–825.

[21] Crasto Noelle, Kirubarajan Abirami, Sussman Dafna. Anthropomorphic brain phantoms for use in MRI systems: a systematic review *Magnetic Resonance Materials in Physics, Biology and Medicine.* 2022;35:277–289.

[22] Fieremans Els, Lee Hong-Hsi. Physical and numerical phantoms for the validation of brain microstructural MRI: A cookbook *NeuroImage.* 2018;182:39–61.

[23] Liu S, Brisset J, Hu J, Haacke EM, Ge Y. Susceptibility weighted imaging and quantitative susceptibility mapping of the cerebral vasculature using ferumoxytol *Journal of Magnetic Resonance Imaging.* 2018;47:621–633.

[24] Han SH, Cho JH, Jg HS, et al. Robust MR assessment of cerebral blood volume and mean vessel size using SPION-enhanced ultrashort echo acquisition *NeuroImage.* 2015;112:382–389.

[25] Michaelis L, Coryell CD, Granick S. Ferritin: III. The magnetic properties of ferritin and some other colloidal ferric compounds *Journal of Biological Chemistry.* 1943;148:463–480.

[26] Macpherson P, Matheson MS. Comparison of calcification of pineal, habenular commissure and choroid plexus on plain films and computed tomography *Neuroradiology.* 1979;18:67–72.

[27] Du Boulay G. *Principles of X-ray Diagnosis of the Skull*. Butterworth-Heinemann2nd ed. 2016.

[28] Baconnier S, Lang SB. Calcite microcrystals in the pineal gland of the human brain: second harmonic generators and possible piezoelectric transducers *IEEE Transactions on Dielectrics and Electrical Insulation.* 2004;11:203–209.

[29] Cheng Yu-Chung N.. Development and Testing of Iron Based Phantoms as Standards for the Diagnosis of Microbleeds and Oxygen Saturation with Applications in Dementia, Stroke, and Traumatic Brain Injury Annual Report ADA601806Defense Technical Information CenterDetroit, Michigan 2013.

[30] Ianniello C, Zwart JA, Duan Q, et al. Synthesized tissue-equivalent dielectric phantoms using salt and polyvinylpyrrolidone solutions *Magnetic resonance in medicine.* 2018;80:413–419.

[31] Rogers JJ. Characterization of Phased Array Coils for Diagnostic Magnetic Resonance Images Tech. Rep. MS 9-2008 (R2014, R2020)NEMA 2021.

[32] Eckstein K, Dymerska B, Bachrata B, et al. Computationally efficient combination of multi-channel phase data from multi-echo acquisitions (ASPIRE) *Magnetic resonance in medicine.* 2018;79:2996–3006.

[33] Chan K, Marques JP. SEPIA—Susceptibility mapping pipeline tool for phase images *Neuroimage.* 2021;227:117611.

[34] Dymerska B, Eckstein K, Bachrata B, et al. Phase unwrapping with a rapid opensource minimum spanning tree algorithm (ROMEO) *Magnetic resonance in medicine.* 2021;85:2294–2308.

[35] Li W, Wu B, Liu C. Quantitative susceptibility mapping of human brain reflects spatial variation in tissue composition *NeuroImage.* 2011;55:1645–1656.

[36] Wu B, Li W, Guidon A, Liu C. Whole brain susceptibility mapping using compressed sensing *Magnetic resonance in medicine.* 2012;67:137–147.

[37] Pei M, Nguyen TD, Thimmappa ND, et al. Algorithm for fast monoexponential fitting based on Auto-Regression on Linear Operations (ARLO) of data: T2* Mapping Using ARLO *Magnetic Resonance in Medicine.* 2015;73:843–850.

[38] Yushkevich PA, Piven J, Hazlett HC, et al. User-guided 3D active contour segmentation of anatomical structures: Significantly improved efficiency and reliability *NeuroImage.* 2006;31:1116–1128.

[39] Wang Y, Tadimalla S, Rai R, et al. Quantitative MRI: Defining repeatability, reproducibility and accuracy for prostate cancer imaging bioMer development *Magnetic Resonance Imaging.* 2021;77:169–179.

[40] McGraw Kenneth O, Wong Seok P. Forming inferences about some intraclass correlation coefficients. *Psychological methods.* 1996;1:30-46.

[41] Koo Terry K., Li Mae Y.. A Guideline of Selecting and Reporting Intraclass Correlation Coefficients for Reliability Research *Journal of Chiropractic Medicine.* 2016;15:155–163.

[42] Olsson Emma, Wirestam Ronnie, Lind Emelie. MRI-Based Quantification of Magnetic Susceptibility in Gel Phantoms: Assessment of Measurement and Calculation Accuracy *Radiology Research and Practice.* 2018;2018:1–13.

[43] Neelavalli Jaladhar, Cheng Yu-Chung Norman. *Magnetic Susceptibility*:17–31. John Wiley & Sons, Inc.

[44] Zhou Dong, Cho Junghun, Zhang Jingwei, Spincemaille Pascal, Wang Yi. Susceptibility underestimation in a high-susceptibility phantom: Dependence on imaging resolution, magnitude contrast, and other parameters: QSM Estimation Dependence on Resolution, Magnitude Contrast, and Other Parameters *Magnetic Resonance in Medicine.* 2017;78:1080–1086.

[45] Emmerich J, Bachert P, Ladd ME, Straub S. A novel phantom with dia- and paramagnetic substructure for quantitative susceptibility mapping and relaxometry *Physica Medica.* 2021;88:278–284.

[46] Cuña Enrique Gustavo, Schulz Hildegard, Tuzzi Elisa, et al. Simulated and experimental phantom data for multi-center quality assurance of quantitative susceptibility maps at 3 T, 7 T and 9.4 T *Physica Medica: European Journal of Medical Physics.* 2023;110.

[47] Hooper P, Tourell M, O'Brien K, Jin J, Robinson SD, Barth M. Development of a Quantitative Susceptibility Mapping (QSM) phantom for validation of acquisition strategies and post-processing tools at 3 T Proc Intl Soc Mag Reson Med(London, England, UK) 2022. Abstract 1983.

[48] Williams JH. *Quantifying Measurement: The Tyranny of Numbers*. San Rafael, CA, USA: Morgan & Claypool Publishers 2016.

Table 1: Acquisition, online reconstruction parameters and head coil used on the MR scanners.

Table 2: Intra-session and inter-session repeatability measurements. Interclass coefficient (ICC) was expressed as a 95 % confidence interval.

Table 3: Relaxivity estimates for the 4 materials. Relaxivity and intercept were given as point estimate (95% confidence interval).

Figure 1: A, Internal phantom structure. 20 NMR vials are supported by custom-made acrylic supports. B, Top view of phantom showing a small hole for removing bubbles into the trapping zone. C, CAD model of the phantom fitting within the tight-fitting 7 Tesla Nova Medical 32 Rx-element coil. The phantom was aligned parallel to the magnetic field. Firm sandbags were placed around the phantom to centre it within the head coil.

Figure 2: Imaging artefacts in earlier phantom prototypes. A-D: Axial view, $R2^*$ and QSM maps at 3 Tesla of various vial thicknesses. A,B: 10 mm vial (0.3 mm wall thickness), vial wall effects not observed. C,D: 15 mm vial (2.0 mm wall thickness), at vial wall observed high $R2^*$ values and erroneous QSM values. E,F: Magnitude images at 7 Tesla showing inhomogeneity at the base of the phantom due to incorrectly too low (E) and correctly elevated (F) within the head coil. G,H: 7 Tesla magnitude and field map showing standing waves, due to shorter RF wavelengths due to uncorrected electric permittivity. I,J: 7 Tesla magnitude and field map showing chemical shift artefacts due to lipids within the phantom. K,L: typical QSM maps of the final phantom at 3 T and 7 T, respectively.

Figure 3: A & B, QSM and $R2^*$ maps as a function of USPIO concentration. The windowing of the QSM map at 7 T was set to half that of 3 T. The red arrow indicates the presence of an agglomerate in the 0.448 μM ROI, manifesting as bright in both the QSM and $R2^*$ maps. C & D, Scatter plots of QSM and $R2^*$ as a function of USPIO concentration.

Figure 4: A & B, QSM and $R2^*$ maps as a function of ferritin concentration. The ferritin agglomerates were indicated with a red arrow on the $R2^*$ maps and were corresponding to 6.98, 8.60, 10.21 μM ROIs, manifesting as dark in the QSM map and bright on the 7 T $R2^*$ map. C & D, Scatter plots of QSM and $R2^*$ as a function of ferritin concentration.

Figure 5: A & B, QSM and $R2^*$ maps as a function of concentration of calcium chloride ($CaCl_2$). The voxels corresponding to $CaCl_2$ 4.5 mM were heterogeneous, as indicated with a red arrow on the 7 T QSM map. Shading at phantom periphery due to the interaction between $CaCl_2$ conductivity and the B_1 field was indicated with a red arrow on the 7 T $R2^*$ map. C & D, Scatter plots of QSM and $R2^*$ as a function of concentration of $CaCl_2$.

Figure 6: A & B, QSM maps and variation in QSM values as a function of concentration of calcium carbonate ($CaCO_3$). $R2^*$ maps and variation in $R2^*$ values as a function of $CaCO_3$. At both 3 T and 7 T, 1 mM contained diamagnetic clumps (dark on QSM map, bright on R2* map) surrounded by a paramagnetic mixture (bright on QSM map, dark on R2* map). C & D, Scatter plots of QSM and $R2^*$ as a function of concentration of $CaCO_3$.

Table S1: Signal-to-Noise-Ratio (SNR) from TE = 1.87 to 22.44 ms at 3 Tesla

Table S2: Signal-to-Noise-Ratio (SNR) from TE = 3.15 to 28.35 ms at 7 Tesla

Table S3: Analytical Chi and QSM measurements for the 5 ferritin ROIs. The local field, QSM and analytical chi were expressed as mean (std).

Figure S1: Scatter plots of QSM, chi analytical and reference susceptibility as a function of ferritin

concentration at (A) 3 T and at (B) 7 T.

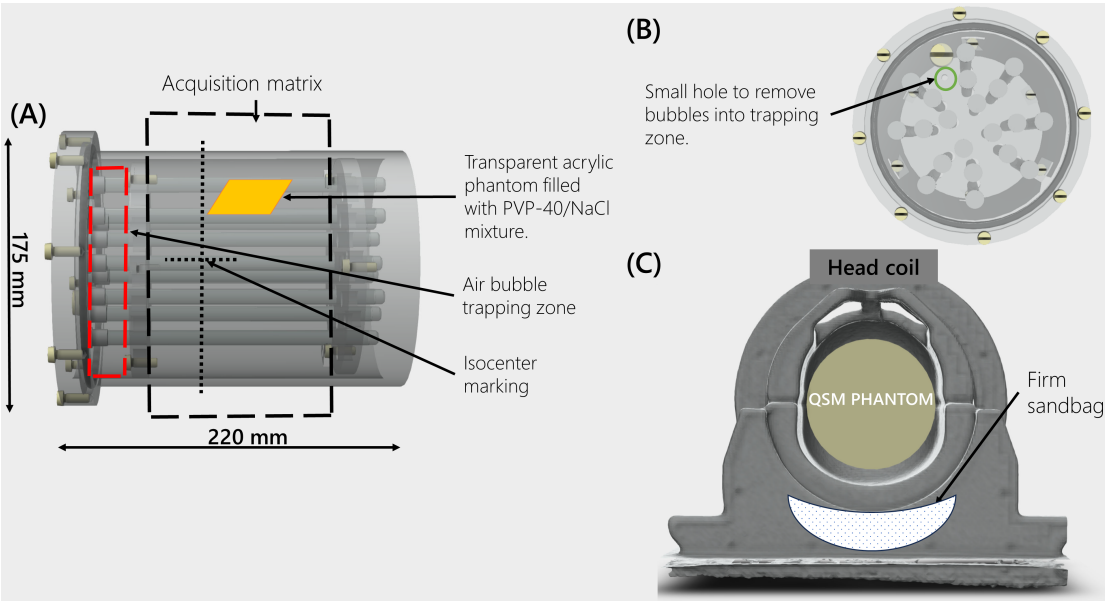

Figure 1: A, Internal phantom structure. 20 NMR vials are supported by custom-made acrylic supports. B, Top view of phantom showing a small hole for removing bubbles into the trapping zone. C, CAD model of the phantom fitting within the tight-fitting 7 Tesla Nova Medical 32 Rx-element coil. The phantom was aligned parallel to the magnetic field. Firm sandbags were placed around the phantom to centre it within the head coil.

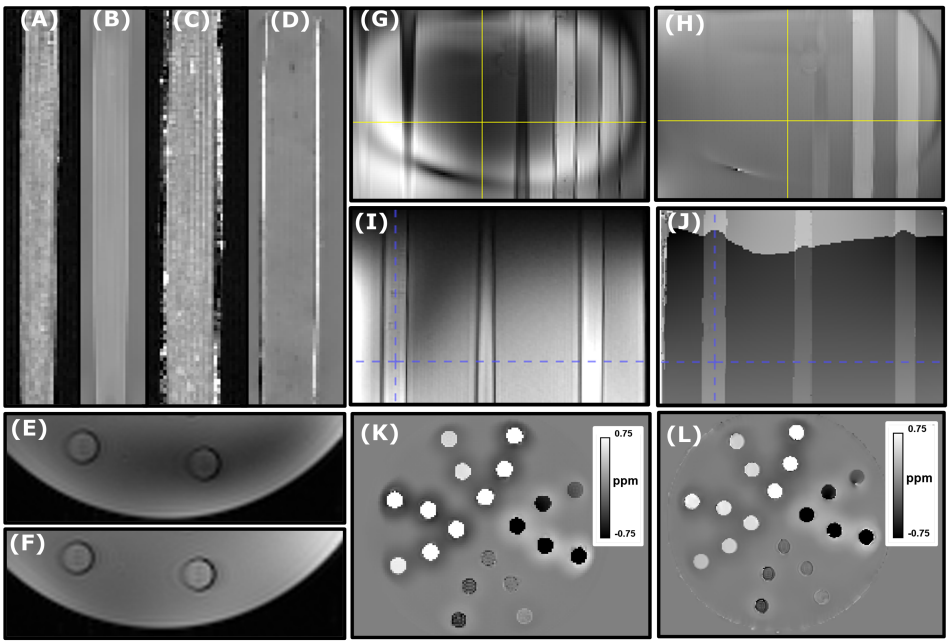

Figure 2: Imaging artefacts in earlier phantom prototypes. A-D: Axial view, $R2^*$ and QSM maps at 3 Tesla of various vial wall thicknesses. A,B: 10 mm vial (0.3 mm wall thickness), vial wall effects not observed. C,D: 15 mm vial (2.0 mm wall thickness), at vial wall observed high $R2^*$ values and erroneous QSM values. E,F: Magnitude images at 7 Tesla showing inhomogeneity at the base of the phantom due to incorrectly too low (E) and correctly elevated (F) within the head coil. G,H: 7 Tesla magnitude and field map showing standing waves, due to shorter RF wavelengths due to unsuitable electric permittivity. I,J: 7 Tesla magnitude and field map showing chemical shift artefacts due to lipids within the phantom. K,L: typical QSM maps of the final phantom at 3 T and 7 T, respectively.

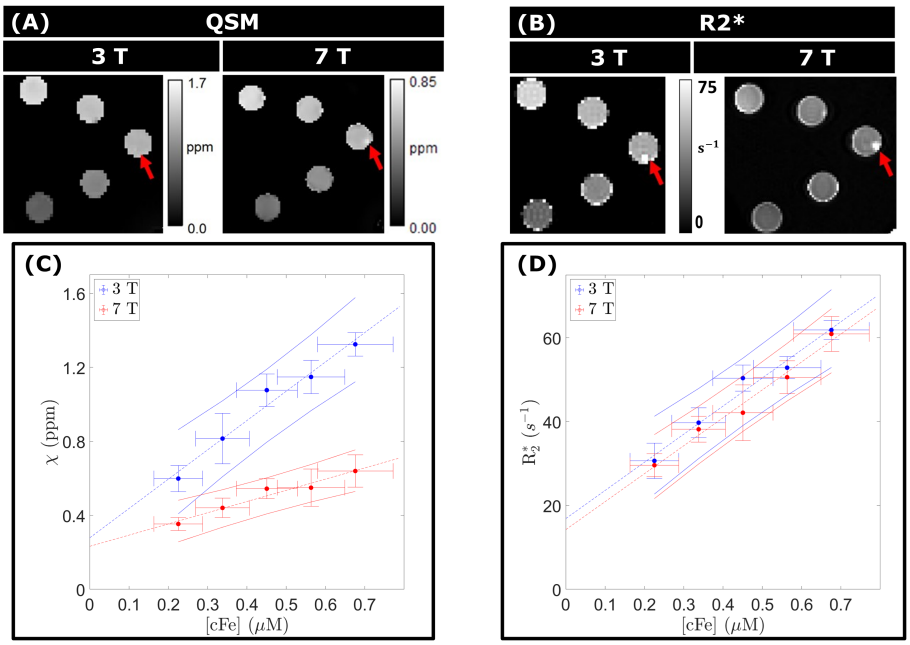

Figure 3: A & B, QSM and $R2^*$ maps as a function of USPIO concentration. The windowing of the QSM map at 7 T was set to half that of 3 T. The red arrow indicates the presence of an agglomerate in the 0.448 μM ROI, manifesting as bright in both the QSM and $R2^*$ maps. C & D, Scatter plots of QSM and $R2^*$ as a function of USPIO concentration.

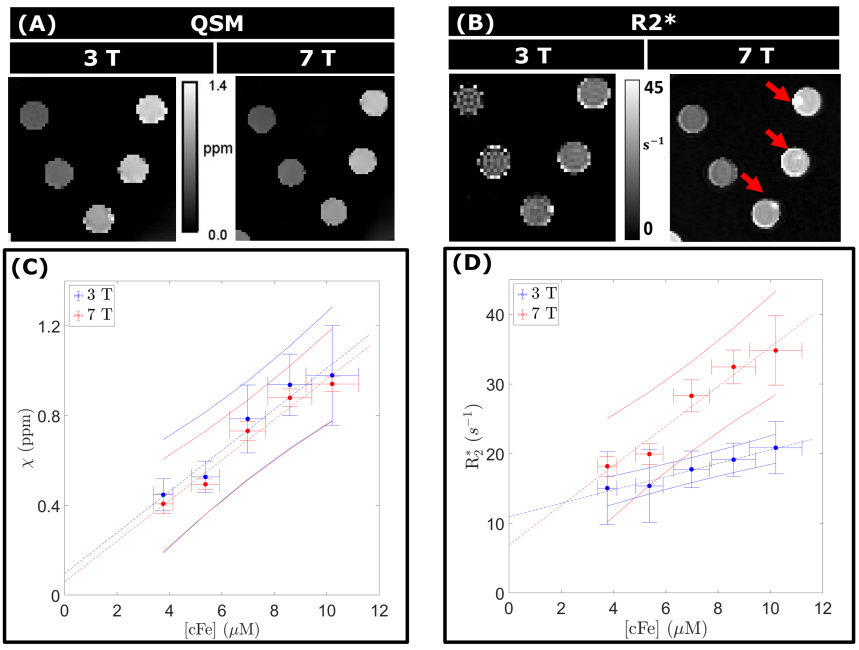

Figure 4: A & B, QSM and $R2^*$ maps as a function of ferritin concentration. The ferritin agglomerates were indicated with a red arrow on the $R2^*$ maps and were corresponding to 6.98, 8.60, 10.21 μM ROIs, manifesting as dark in the QSM map and bright on the 7 T $R2^*$ map. C & D, Scatter plots of QSM and $R2^*$ as a function of ferritin concentration.

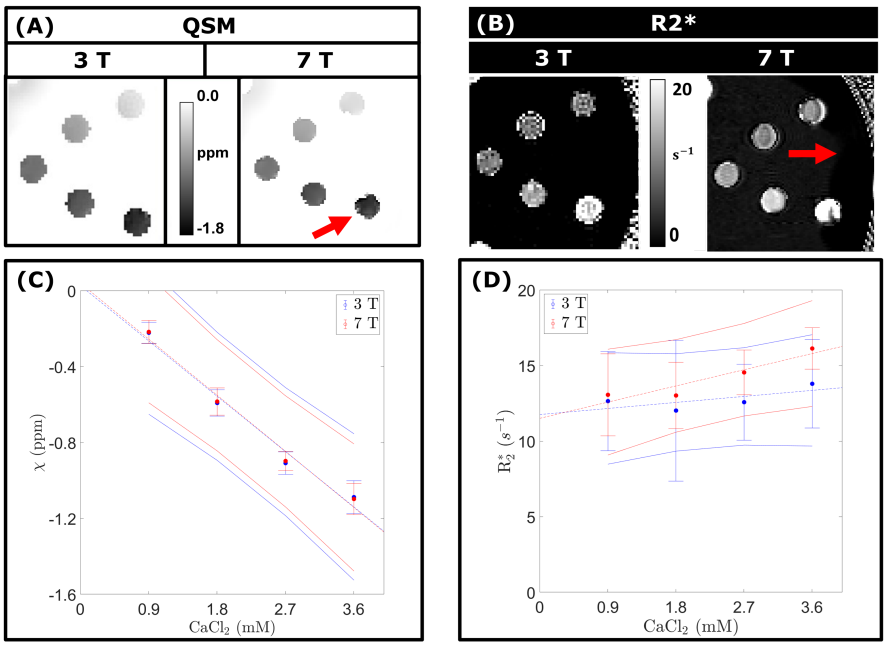

Figure 5: A & B, QSM and $R2^*$ maps as a function of concentration of calcium chloride ($CaCl_2$). The voxels corresponding to $CaCl_2$ 4.5 mM were heterogeneous, as indicated with a red arrow on the 7 T QSM map. Shading at phantom periphery due to the interaction between $CaCl_2$ conductivity and the B_1 field was indicated with a red arrow on the 7 T $R2^*$ map. C & D, Scatter plots of QSM and $R2^*$ as a function of concentration of $CaCl_2$.

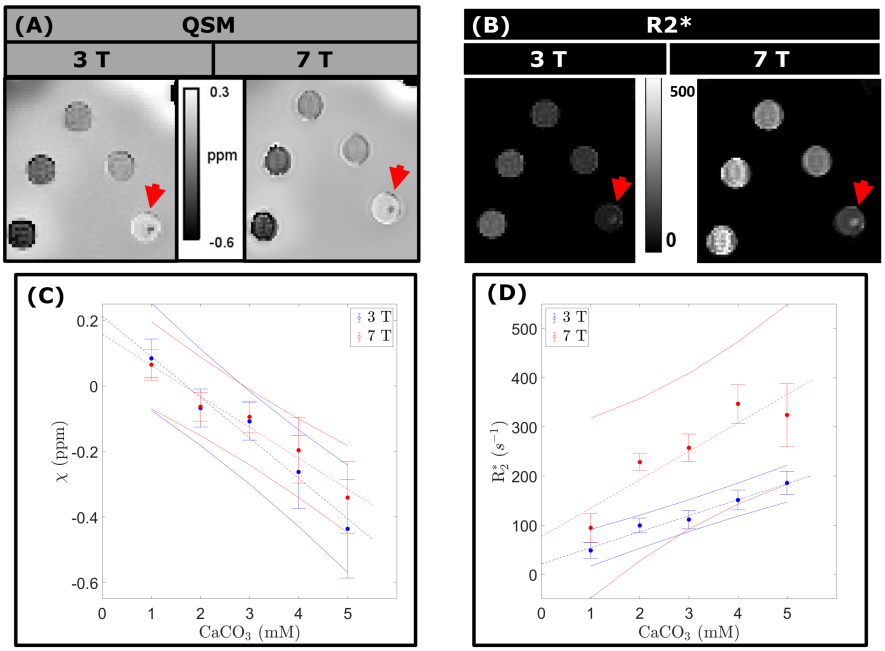

Figure 6: A & B, QSM maps and variation in QSM values as a function of concentration of calcium carbonate ($CaCO_3$). $R2^*$ maps and variation in $R2^*$ values as a function of $CaCO_3$. At both 3 T and 7 T, 1 mM contained diamagnetic clumps (dark on QSM map, bright on R2* map) surrounded by a paramagnetic mixture (bright on QSM map, dark on R2* map). C & D, Scatter plots of QSM and $R2^*$ as a function of concentration of $CaCO_3$.

A Sample concentration and uncertainties

A.1 Iron-based phantoms

Molar iron concentration (c_{Fe}) was formulated as:

$$c_{Fe} = \frac{V_{Solution} \times c_{Solution}}{V_w \times M_{Fe}} \tag{1}$$

including the solution volume ($V_{Solution}$, mL), the solution iron concentration ($c_{Solution}$, mg.mL^{-1}) and deionized water volume (V_w, mL). The molar mass of iron $M_{Fe} = 55.845$ g/mol was treated as a constant.

Since the measurements were multiplied and divided by, their uncertainties were propagated[48]. The uncertainty of iron concentration $u(c_{Fe})$ was then formulated by root sum-of-squares:

$$\frac{u(c_{Fe})}{c_{Fe}} = \sqrt{\left[\frac{u(V_{Solution})}{V_{Solution}}\right]^2 + \left[\frac{u(c_{Solution})}{c_{Solution}}\right]^2 + \left[\frac{u(V_w)}{V_w}\right]^2} \tag{2}$$

For both iron-based phantoms, the relative uncertainties $u(c_{Fe})/c_{Fe}$ were greater than or equal to 10%. The calculated uncertainties were indicated as an error term on the scatter plots in Figure 3& 4.

A.2 Calcium-based phantoms

Molar concentration (c) was formulated as:

$$c = \frac{m_{powder}}{V_w \times M} \tag{3}$$

including the calcium-based powder mass (m_{powder}, grams), and the deionized water volume (V_w, mL). The molar masses of calcium chloride $M_{CaCl2} = 110.98$ g/mol and calcium carbonate $M_{CaCO3} = 100.09$ g/mol were substituted for M and treated as constants.

The uncertainty of the concentration $u(c)$ was formulated as:

$$\frac{u(c)}{c} = \sqrt{\left[\frac{u(m_{powder})}{m_{powder}}\right]^2 + \left[\frac{u(V_w)}{V_w}\right]^2} \tag{4}$$

For both calcium-based phantoms, the relative uncertainties $u(c)/c$ were each less than 1%, and were thus excluded from Figures 5& 6.

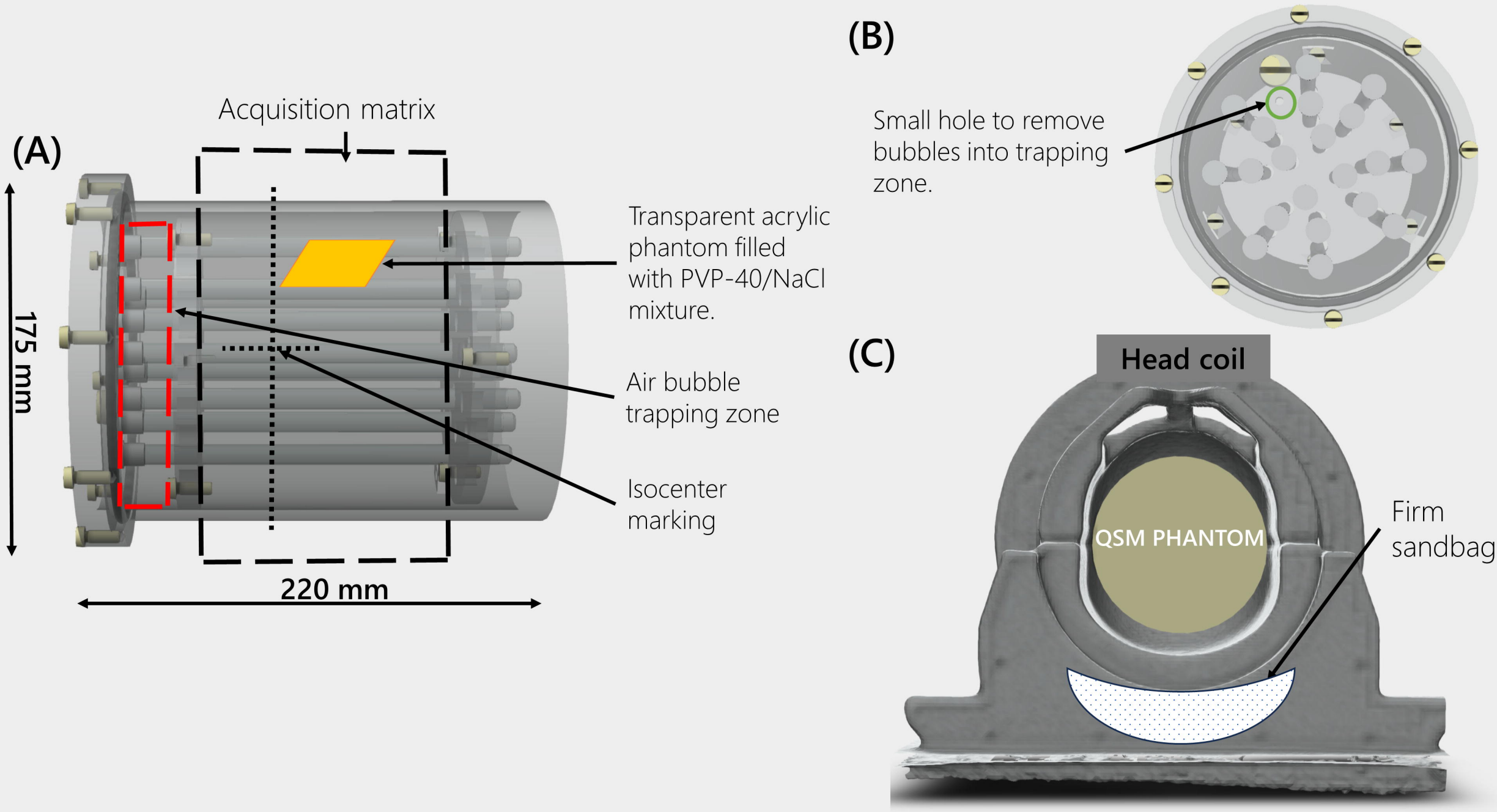
(A)
Acquisition matrix
Transparent acrylic phantom filled with PVP-40/NaCl mixture.
Air bubble trapping zone
Isocenter marking
175 mm
220 mm
(B)
Small hole to remove bubbles into trapping zone.
(C)
Head coil
QSM PHANTOM
Firm sandbag

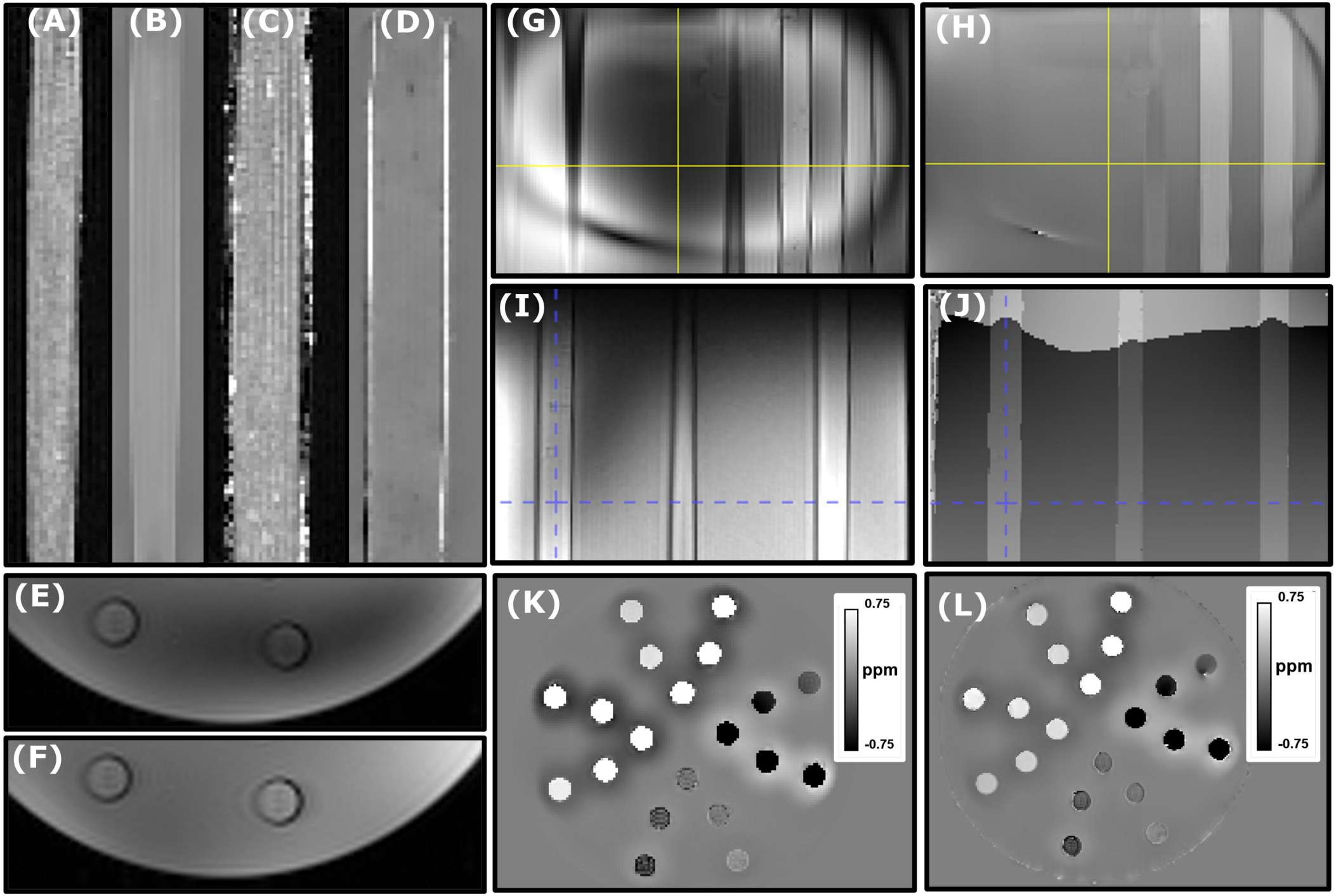
(A)
(B)
(C)
(D)
(G)
(H)
(I)
(J)
(E)
(F)
(K)
0.75
ppm
-0.75
(L)
0.75
ppm
-0.75

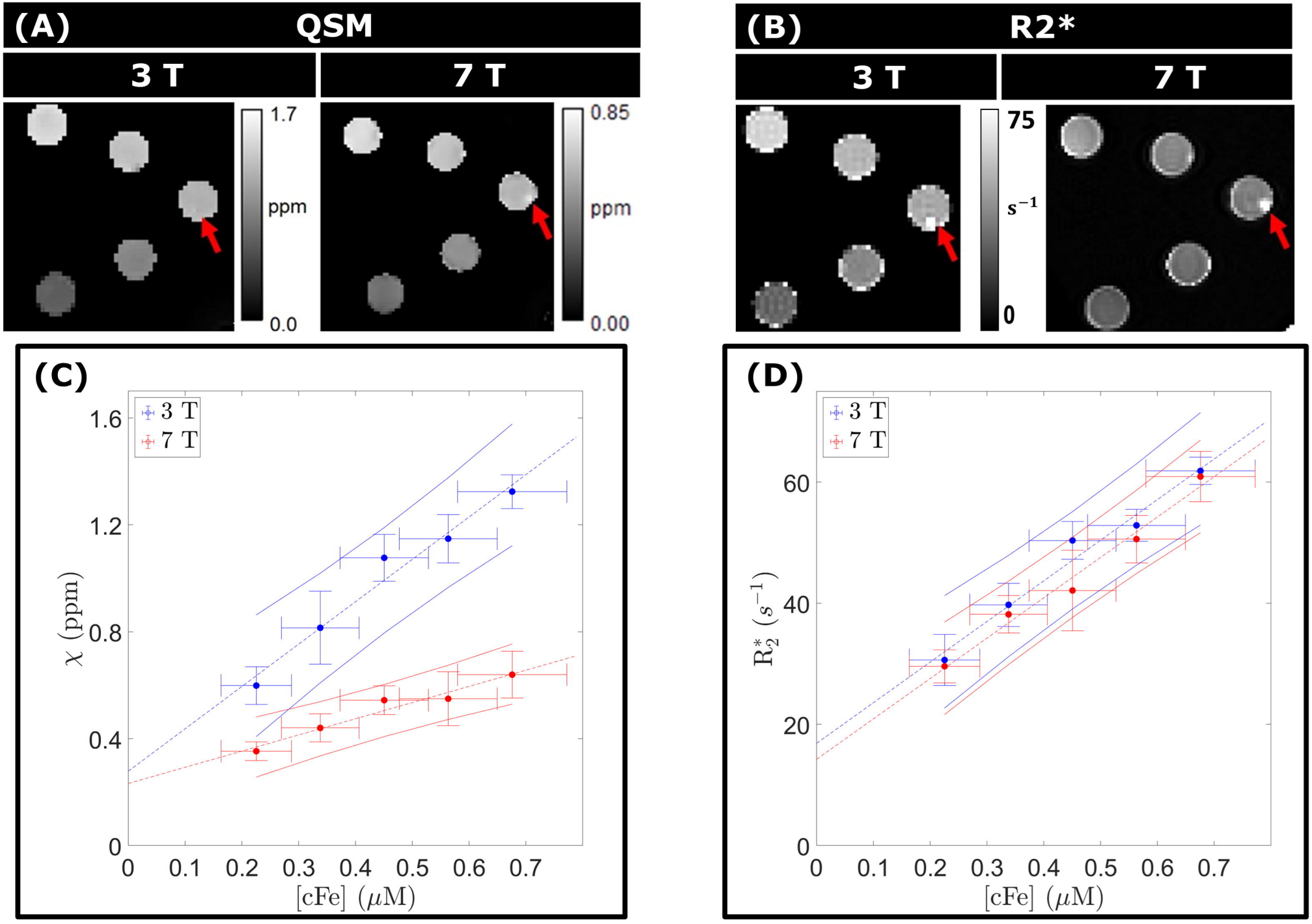
(A)
QSM
3 T
7 T
1.7
ppm
0.0
0.85
ppm
0.00
(B)
R2*
3 T
7 T
75
s^{-1}
0
(C)
3 T
7 T
χ (ppm)
[cFe] (μM)
(D)
3 T
7 T
R_2^* (s^{-1})
[cFe] (μM)

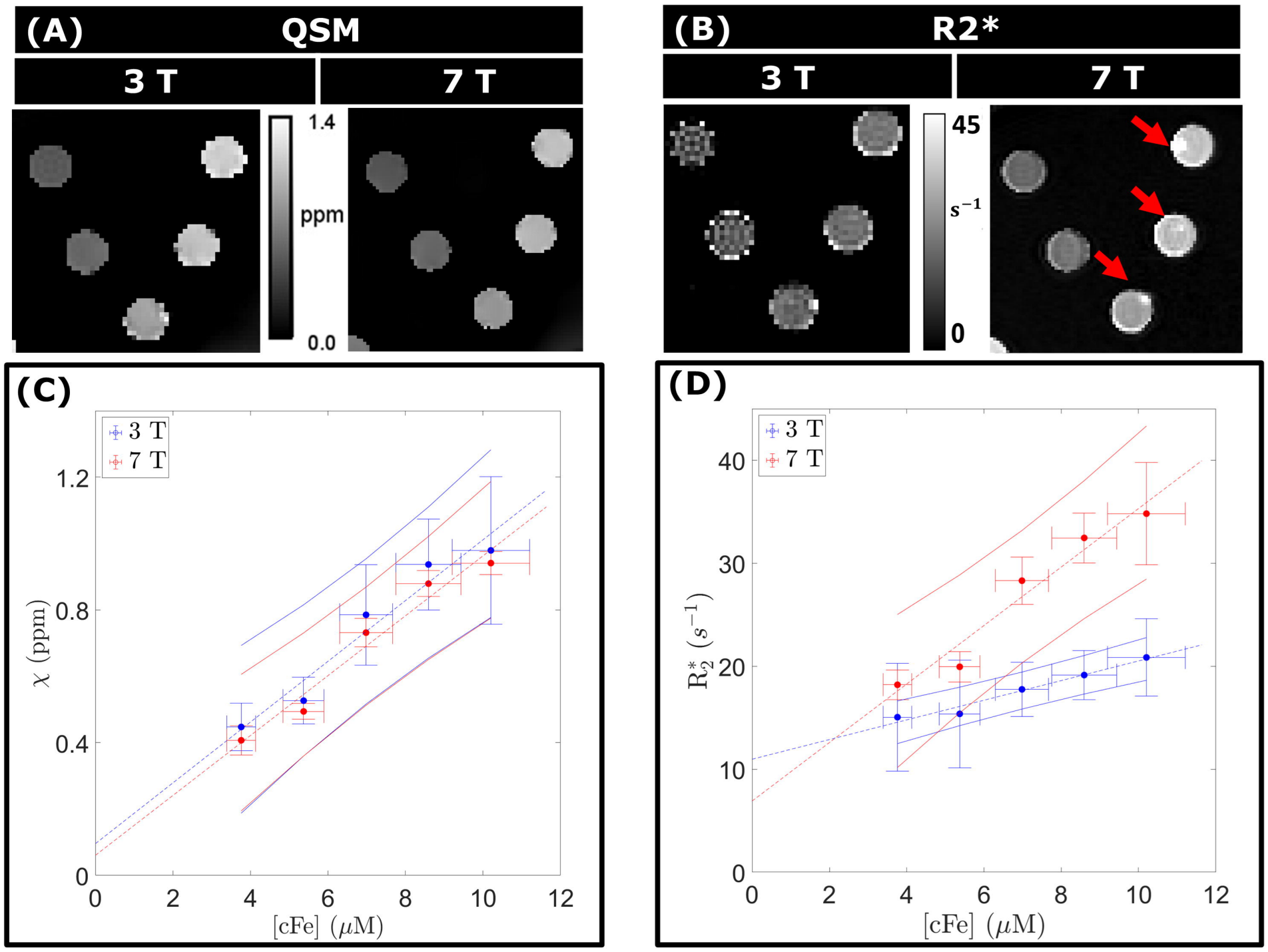
(A)
QSM
3 T
7 T
1.4
ppm
0.0
(B)
R2*
3 T
7 T
45
s^{-1}
0
(C)
3 T
7 T
χ (ppm)
[cFe] (μM)
(D)
3 T
7 T
R_2^* (s^{-1})
[cFe] (μM)

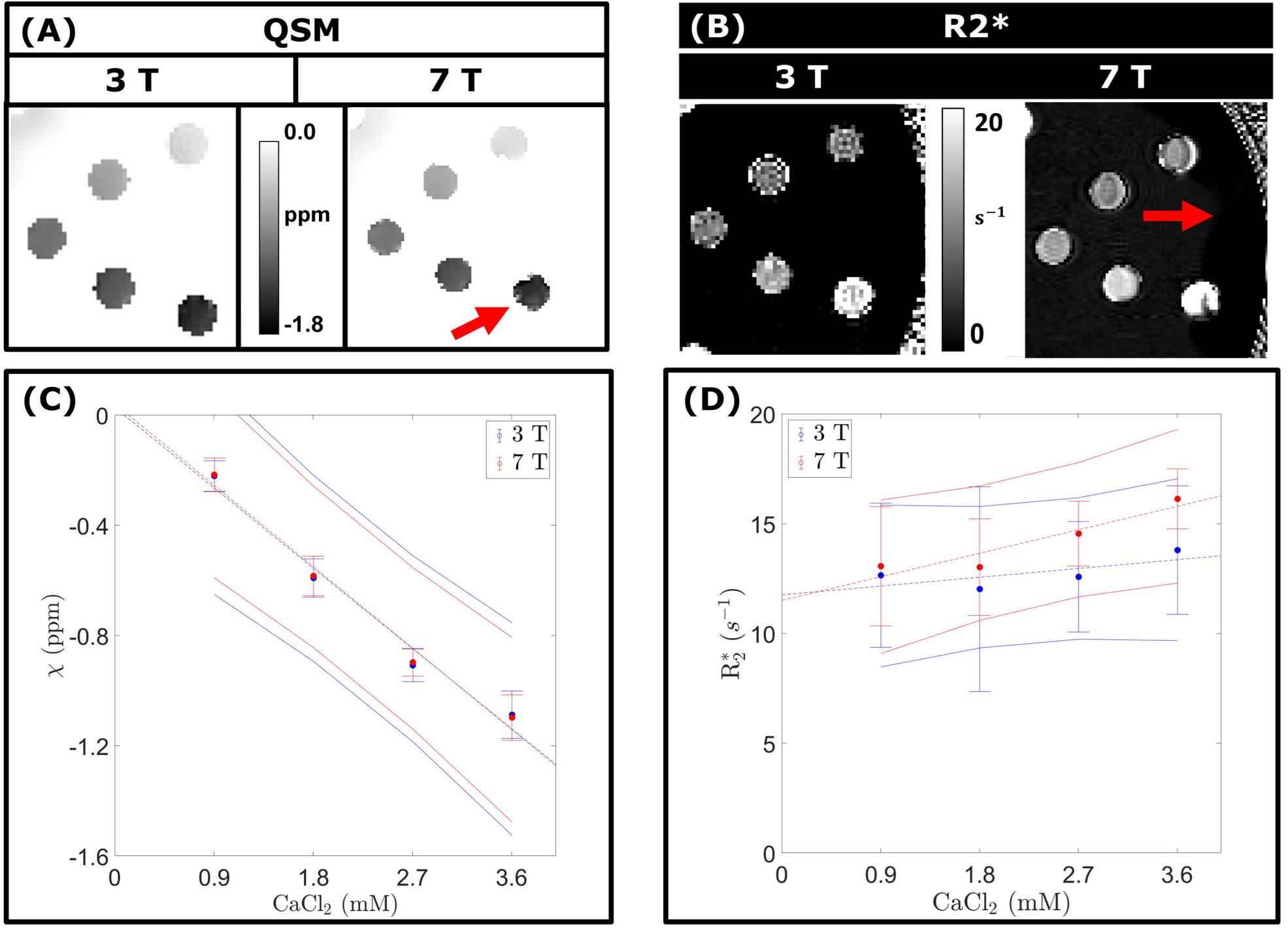
(A)
QSM
3 T
7 T
0.0
ppm
-1.8
(B)
R2*
3 T
7 T
20
s^{-1}
0
(C)
3 T
7 T
χ (ppm)
0
-0.4
-0.8
-1.2
-1.6
0
0.9
1.8
2.7
3.6
$CaCl_2$ (mM)
(D)
3 T
7 T
R_2^* (s^{-1})
20
15
10
5
0
0
0.9
1.8
2.7
3.6
$CaCl_2$ (mM)

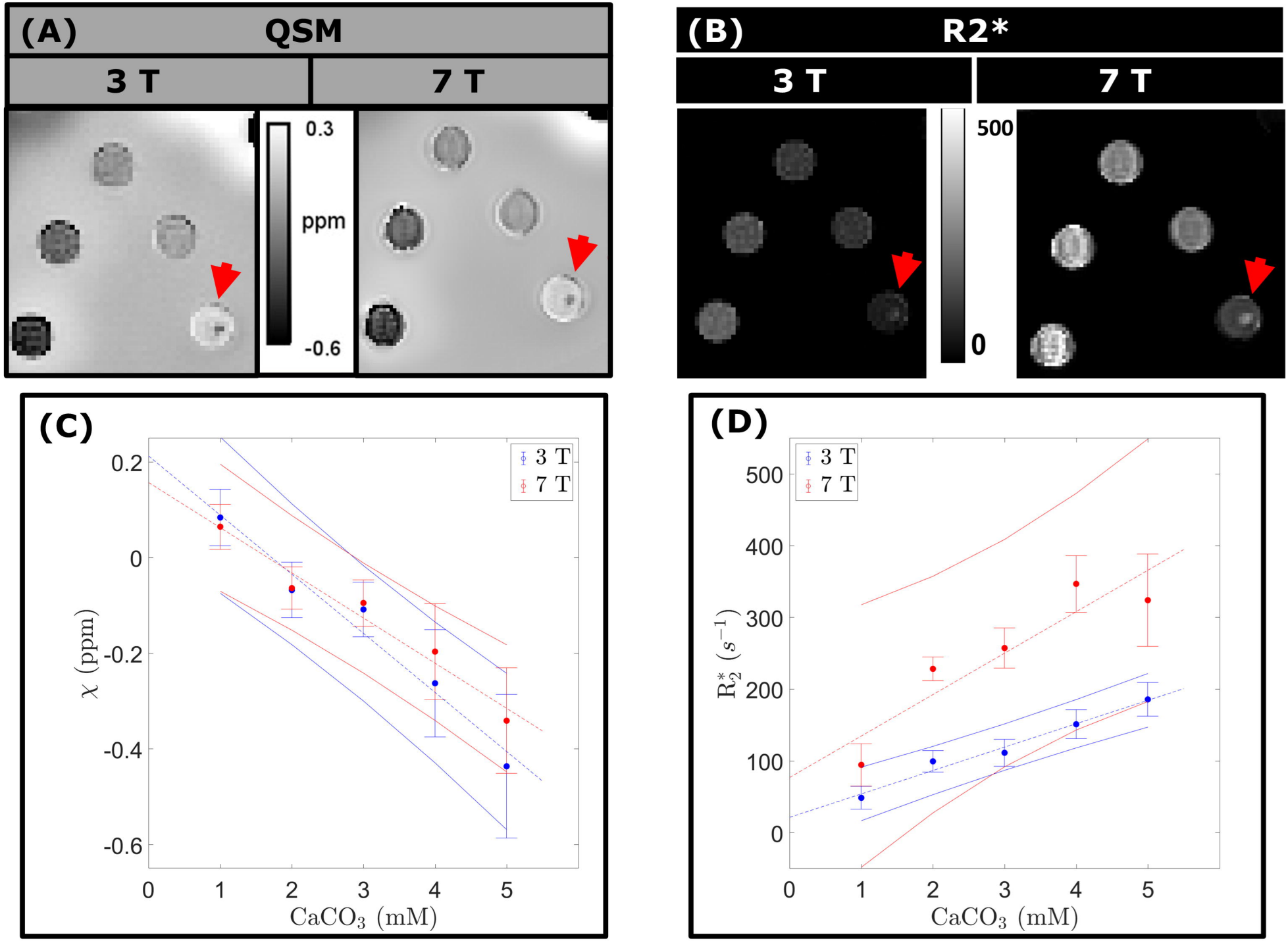
(A)
QSM
3 T
7 T
0.3
ppm
-0.6
(B)
R2*
3 T
7 T
500
0
(C)
3 T
7 T
0.2
0
-0.2
-0.4
-0.6
χ (ppm)
0
1
2
3
4
5
CaCO3 (mM)
(D)
3 T
7 T
500
400
300
200
100
0
R2* (s−1)
0
1
2
3
4
5
CaCO3 (mM)